



Gust forecasting in Uruguay in support of wind energy.

Alejandro Gutierrez Arce¹, Robert G. Fovell²,

¹Instituto de Mecánica de los Fluidos e Ingeniería Ambiental, Facultad de Ingeniería,
Universidad de la República, Montevideo Uruguay.

²Department of Atmospheric and Oceanic Sciences, University of California, Los Angeles, USA.

email: aguti@fing.edu.uy, rfovell@ucla.edu

ABSTRACT: The present work analyzes tower measurements made in Uruguay for wind energy purposes, focusing on forecasting gusts at about 100 m above ground level with targeted WRF simulations. Observed gust magnitudes and gust factors (the ratio of the gusts to the mean winds) both increase as the atmosphere becomes less stable at three towers spanning the nation. Gust factors, however, asymptotically approach 1.33 as the mean wind becomes large. Using an established, theory-based gust parameterization based on mean velocity and friction velocity, we find WRF reasonably reproduces the variation of gust factors with respect to mean wind and stability, but underpredicts significant gust (> 15 m/s) events, with moderate (3.3 km) resolution being adequate for the task. Our analysis suggests that the gust parameterization is skillful but should be modified to be more directly aware of the ambient stability and shear. We propose a new and different strategy that helps capture sizable gusts that occur in marginal stability conditions.

KEY WORDS: Gust; wind energy; forecast.

1 Introduction

We analyze observational data recorded by the National Electric Company of Uruguay (UTE) for their assessment of wind energy resources. UTE has installed a set of towers with anemometers and wind vanes, pyranometers and thermometers distributed throughout the country. Wind measurements are made with cup anemometers (model NRG 40) and wind vanes (model NRG 200P) at various heights, including near 100 m where the turbines are mounted, and care has been taken to determine and remove the tower wake effect. We focus on a subset of those towers, representing three different regions of the country, that are similar with respect to land surface (which consists of open, flat grassland with few isolated obstacles) [1].

The spatial-temporal behavior of wind speed in the UTE network has been analyzed by [2]. Principal component (empirical orthogonal function) analysis identified the three components that represent most of the total variation. In addition, cluster analysis was performed for the daily cycle of the hourly average wind speed to determine three regional classifications of the territory. Towers were selected for the present study based on this regionalization. Another selection criterion was the number of heights at which temperature measurements were made, so that on-site estimates of vertical stability could be made.

The present study focuses on the seasons of the year 2012. The mean, standard deviation and minimum and maximum values were computed for 1-hour intervals from 10-minute data to determine the diurnal cycle. Gusts were determined from 2-sec samples. Separate Weather Research and Forecasting (WRF) model simulations, using the Advanced Research WRF core [3], were made for each tower, consisting of telescoping domains with 30-km, 10-km, 3.3-km, and 1.1-km grid spacings centered on each site. The purpose of this study is to test how well a theory-based gust parameterization captures high-wind events that threaten the wind power network.

2 Tower locations and diurnal cycle of stability in planetary boundary layer.

2.1 Tower locations

Uruguay is dominated by rolling plains and low ranges. Observation towers for wind energy are located in three geographical regions: 1) the region close to the Río de la Plata (an estuary comprising of seawater and freshwater from the Paraná River, one of the world's longest rivers, and its main tributary, the Paraguay River, as well as the Uruguay River), 2) the region close to the Atlantic Ocean, and 3) the more continental region of the country, at least 300 km from the Río de la Plata and the Atlantic Ocean. The towers selected as representative of these regions are Rosendo Mendoza (RM), Jose Ignacio (JI) and Aparacio Saravia (AS), respectively (Table 1). Other towers included in Table 1 are Rocha (RCH) Colonia Rubio (CRU) and McMeekan (MC). Figure 1 shows the location of the towers analyzed in this work, plotted on the topography of Uruguay.

	Code	Lat South	Long West	Wind velocity measurement height (m)	Temperature Measurement (m)
Aparicio Saravia	AS	31,143	56,096	101-80-60	99-5
Colonia Rubio	CRU	31,238	57,465	101-80-60	99-3
Jose Ignacio	JI	34,85	54,735	98-40-12	98-4
Rocha	RCH	34,094	53,65	74-31	12
McMeehan	MC	34,643	56,695	101-81-63,5	100-4
Rosendo Mendoza	RM	34,275	57,553	101-81-63,5	100-2

Table 1. Tower locations and measurement heights.

Tower measurement location in topography

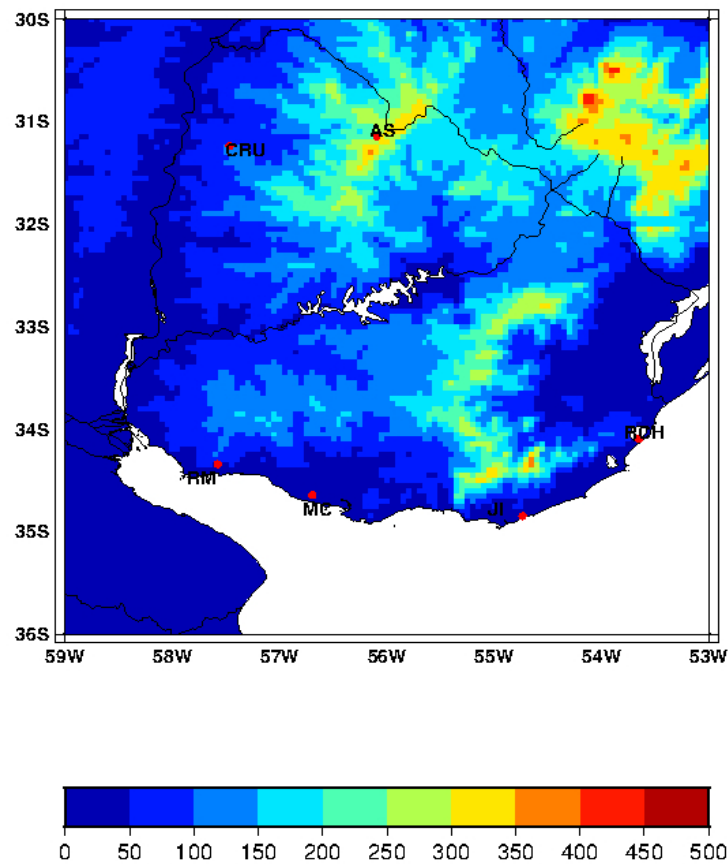


Figure 1 - Locations of six towers considered in this work, and the topography of Uruguay (scale in meters).

2.2 Diurnal cycle of stability in planetary boundary layer.

Wind energy is harvested in the region of the planetary boundary layer where diurnal changes associated with heating and cooling are strong. Additionally, depending on the local topography and distance to the sea, different mesoscale processes are observed. The data analyzed in this work correspond to the terrain of rolling plains. According to [4], the convective layer of the atmosphere grows in height throughout the morning, reaching a height of 1--2 km by mid-afternoon. With the approach of sunset, the capping inversion weakens and becomes patchy as one or more shallow inversion layers form below. At this time, there is a rapid collapse of turbulent motion in the boundary layer as the buoyant plumes that maintain the motion lose their energy source near the surface since the ground cools quickly from radiative heat loss to space.

The diurnal cycle of solar radiation thus determines the condition of stability [5]. There are periodical changes in the vertical structure of the region of the atmosphere analyzed in this work over the course of a day. These changes can be explained by the diurnal cycle of solar radiation, which affects the land-surface heat exchange in the different seasons of the year. There is a transition between a stable condition and unstable condition during sunrise and sunset. The early evening surface-layer transition has been analyzed [6], revealing abrupt changes in this region of the atmosphere observed in the evening under clear skies.

The present work describes the diurnal variations in the gradient of temperature and the gust factor. To analyze the variations in different seasons of the year in terms of the diurnal cycle, the 10-minute data were processed to obtain the mean and maximum value of each variable for each hour in each season. The analysis is presented by season---winter, autumn, spring, and summer---because there are significant changes in solar radiation during the year at latitudes of 30° and 35°S.

The vertical temperature gradient is used as an indicator of stability, and a higher positive value indicates a more strongly stable regime. A superadiabatic temperature gradient indicates a strongly unstable regime. In the 100 m nearest the ground surface, there is no significant height variation in the hydrostatic pressure, and an assumption that the potential temperature is similar to the temperature can be adopted for the differential temperature measurements (using thermometers mounted near tower top and bottom). Figures 2, 3, and 4 show the diurnal variation discriminated by season (summer, autumn, winter and spring) in the vertical gradient of temperature at the RM, AS, and JI towers, in °C/m. The vertical bars show the mean and 16th and 84th percentiles, for the year 2012.

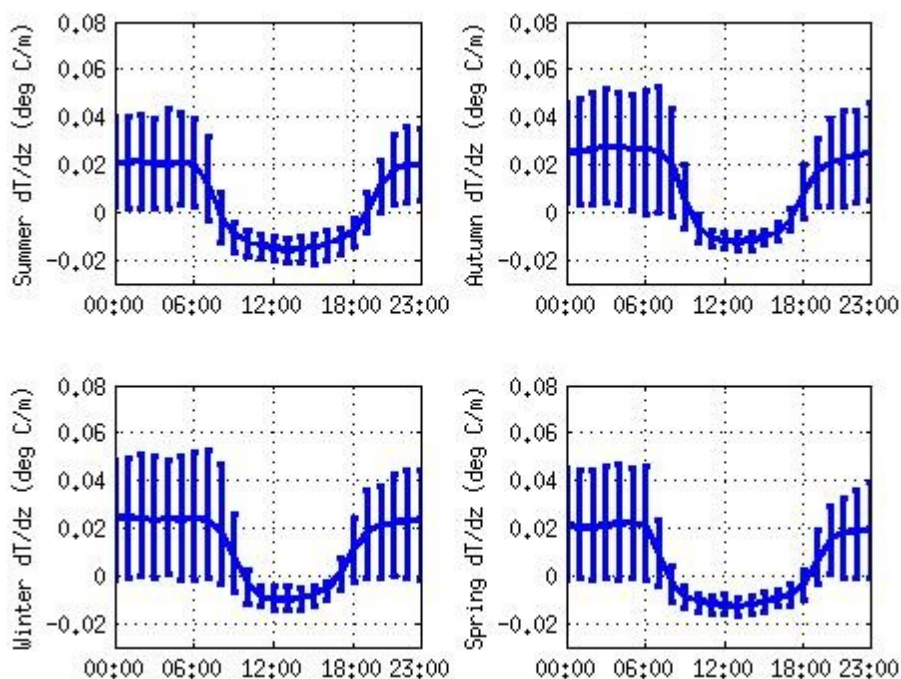


Figure 2 Diurnal variation in the gradient of temperature at the RM tower, at heights between 2 and 100 m, in degrees Celsius per meter. The vertical bars show the mean and 16th and 84th percentiles.

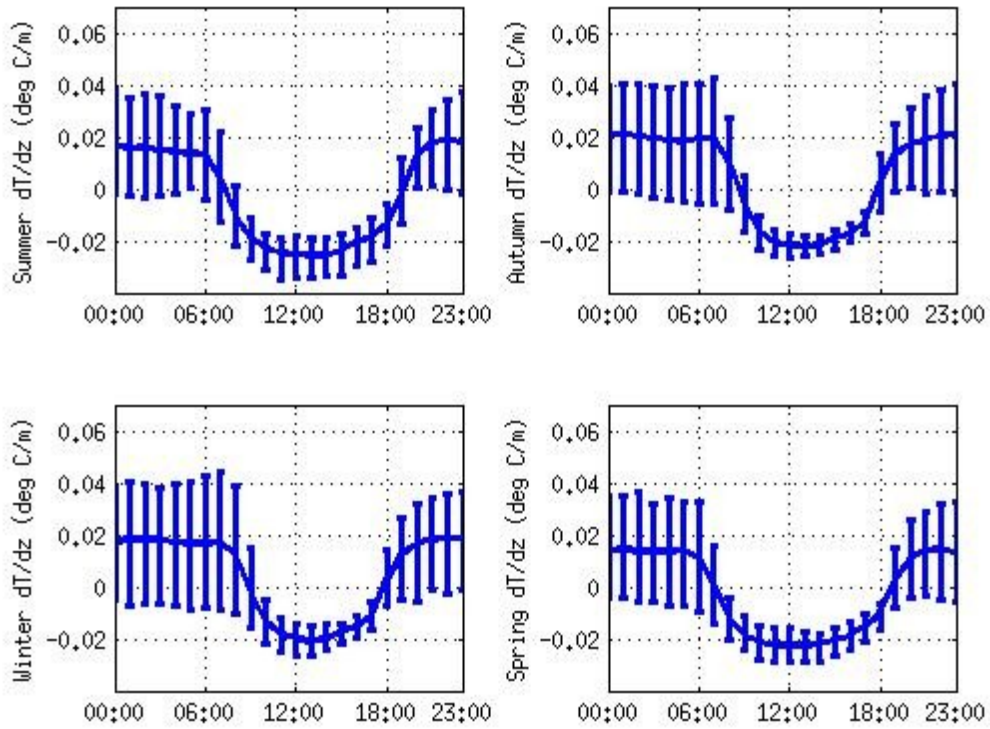


Figure 3 Diurnal variation in the gradient of temperature at the AS tower, at heights between 5 and 99 m, in degrees Celsius per meter. The vertical bars show the mean and 16th and 84th percentiles.

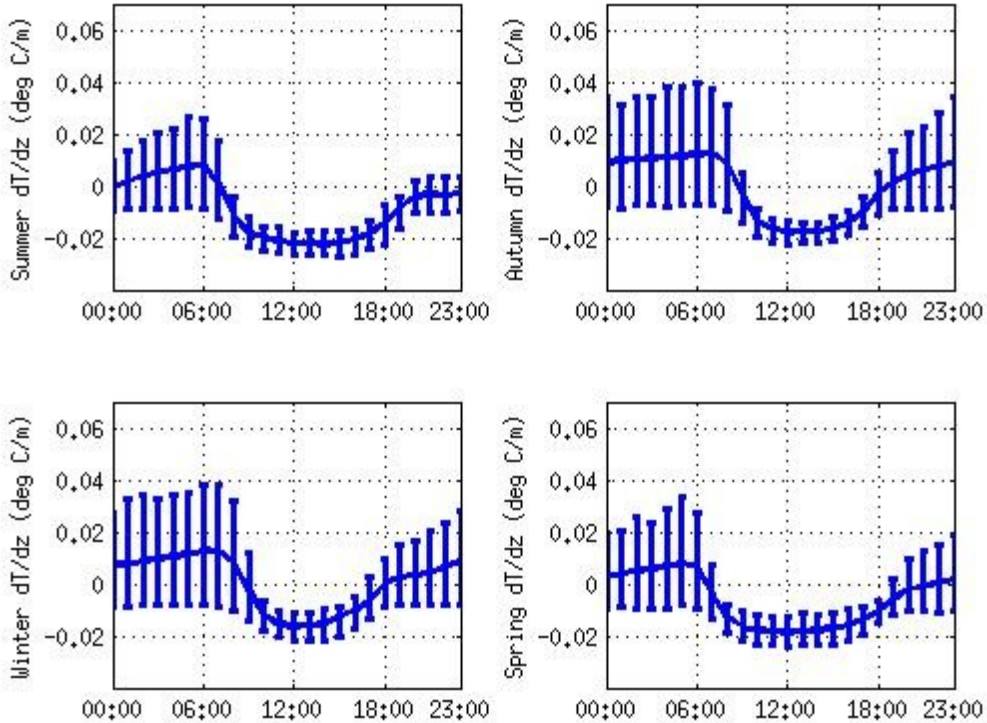


Figure 4 Diurnal variation in the gradient of temperature at the JI tower, at heights between 12 and 98 m, in degrees Celsius per meter. The vertical bars show the mean and 16th and 84th percentiles.

Figures 2-4 show that following sunrise, superadiabatic temperature gradients are frequently observed. A previous study of hourly measurements of temperatures made on a tower between heights of 2 and 32 m in a primarily rural area found 2828 superadiabatic periods over 6 years [7]. Another study observed surface-based superadiabatic and autoconvective layers and concluded that the superadiabatic layers can be long-lived during daytime [8].

In contrast, strong stability is observed at tower locations far from the ocean at night. The sea breeze mixes the air at different levels. Mean values of solar radiation for the analyzed region [9] show that the east coast closer to the ocean receives less radiation during the day, which is related to the higher incidence of cloud cover. If the cloudiness persists into the night, the cloud cover implies less stability in Jose Ignacio than on AS or RM.

For each averaging period (1-h interval), the maximum wind among the 2-sec samples is defined as the gust, g . This gust can be related to the mean (1-h average) wind (V) by the *gust factor*, $GF = g/V$. Figures 5, 6, and 7 present the diurnal variation of the gust factor during 2012 at towers RM, AS and JI, respectively, at the highest height measured, along with the 16th and 84th percentiles. At all three towers, the gust factor is smallest during nighttime when the boundary layer is more stable and resists mixing of higher momentum air downward to anemometer level.

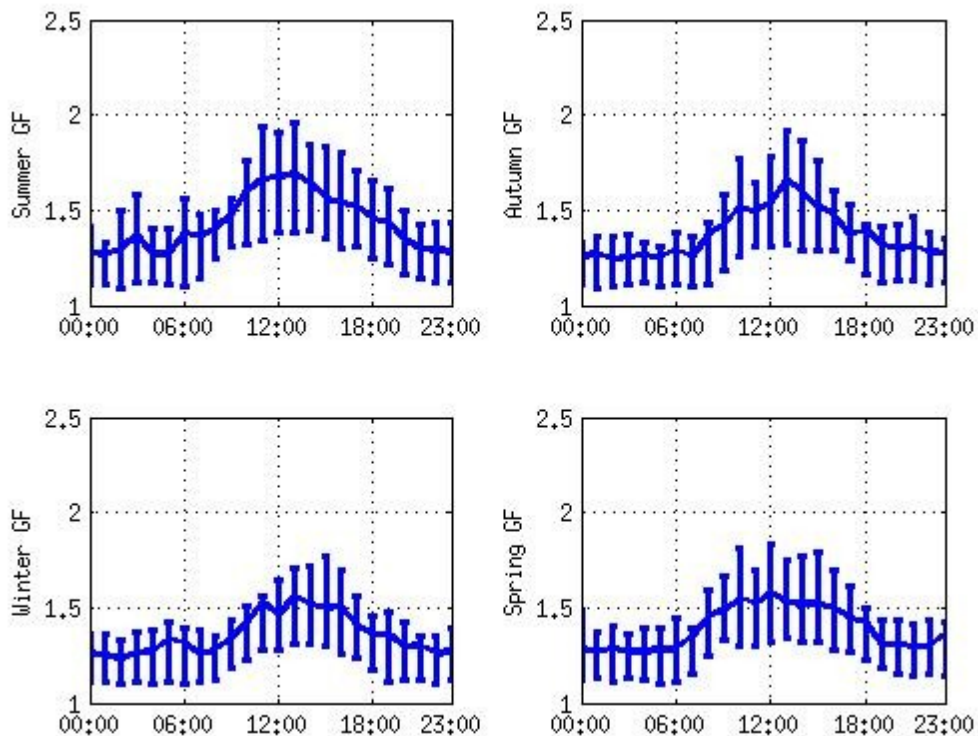


Figure 5 Diurnal variation in the gust factor at the RM tower, at a height of 100 meters. The vertical bars show the mean and 16th and 84th percentiles.

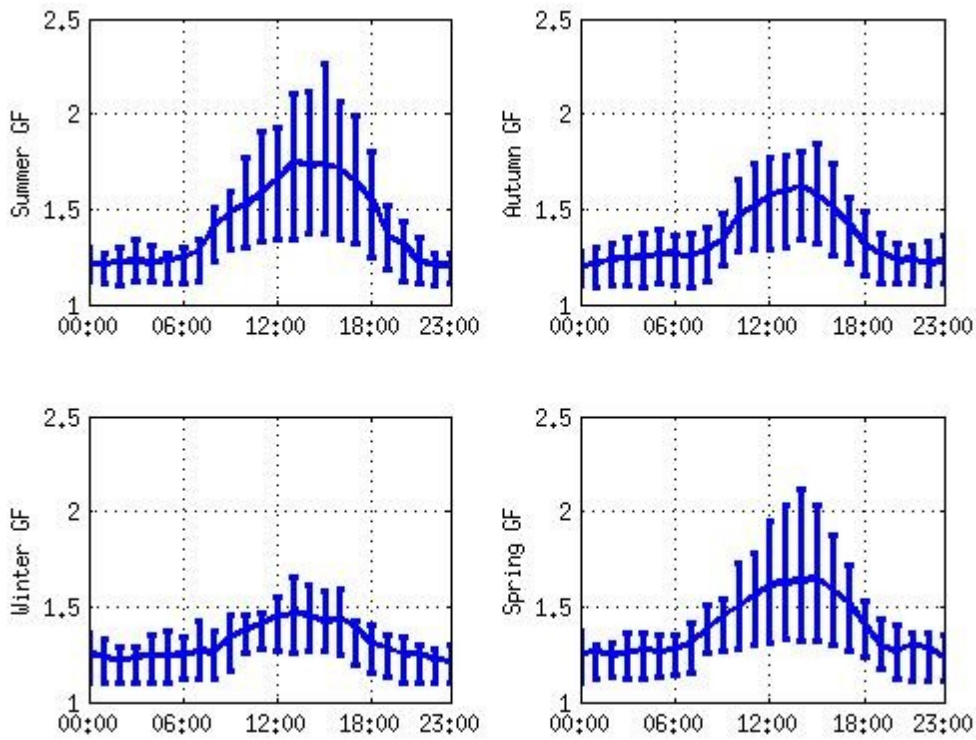


Figure 6 Diurnal variation in the gust factor at the AS tower, at a height of 101 meters. The vertical bars show the mean and 16th and 84th percentiles.

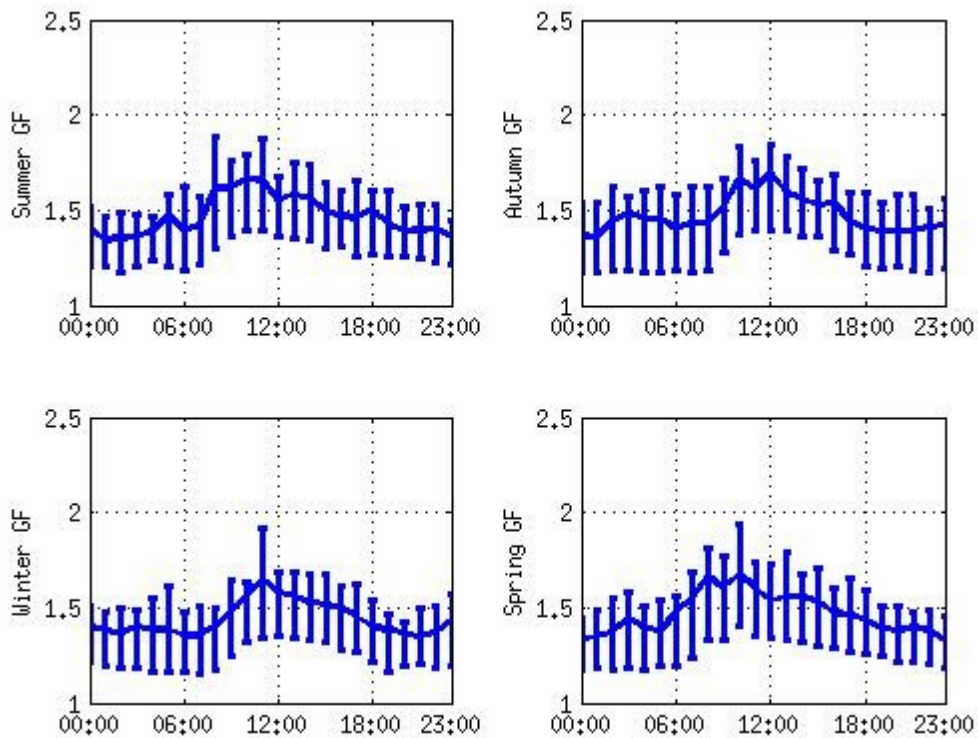


Figure 7 - Diurnal variation in the gust factor at the JI tower, at a height of 98 meters. The vertical bars show the mean and 16th and 84th percentiles.

During the daytime, the gust factor varies more in the seasons with more potentially available solar radiation, which is reasonable because larger instabilities should enhance the generation of turbulent kinetic energy (TKE) [10]. At AS, the most inland tower, GF peaks in the midafternoon hours, during the period in which the boundary layer is least stable (Figure 3), especially during summer. The day-to-day variability is also large, as the site is well protected from the moderating influence of the ocean. The summertime peak is closer to local noon at RM, which is influenced by the nearby Río de la Plata. The variability at JI is suppressed at all hours in all seasons, and tends to reach maximum prior to local noon. This tower is close to the coastline, and is significantly impacted by the sea breeze.

3 Model and methods

3.1 Gust parameterization

The European Center for Medium-Range Weather Forecasts (ECMWF) [11] has presented a gust model based on [5], making the wind gust g a function of mean velocity \bar{V} and friction velocity ust as (1):

$$g = \bar{V} + 7.71 ust \quad (1)$$

The ECMWF employs this equation to estimate the wind gust at 10-m above ground level (AGL). This equation presumes that gusts are non-convective in nature; ECMWF includes an augmentation term when convective activity is expected. We will investigate its applicability to forecasting gusts at turbine level (~100 m), which is typically the top of the surface layer in which the logarithmic wind profile is presumed valid [5].

3.2 WRF simulations

As noted above, nested simulations are targeted to each of the three towers separately. In each model run, the nesting is two-way and the 30-km domain covers a significant portion of South America (not shown), centered on the Rio de la Plata, with the finer domains centered on the tower locations. Separate model runs employing one, two, three and all four domains were made. All simulations utilize 53 vertical layers with the model top at 100 hPa. The lowest model sigma levels are at 1, 0.9987, 0.9974, 0.9948, 0.9922, 0.9896, 0.98693, 0.9843 and 0.9777. Physical parameterizations selected for these runs include the National Center for Atmospheric Research (NCAR) Community Atmospheric Model (CAM) radiation scheme [12], Purdue-Lin microphysics [13], and the Noah land surface model [14]. The Kain-Fritsch [15] cumulus parameterization is employed in the 30- and 10-km domains. The National Centers for Environmental Prediction (NCEP) Global Forecast System (GFS) operational global analyses are used for the initial and boundary conditions. Sensitivity to the number of domains used and the planetary boundary layer scheme (PBL) was assessed, with the Mellor-Yamada-Janjic (MYJ) scheme [16] representing the control configuration examined herein.

4 ECMWF gust model with WRF, discriminated by stability.

Table 2 compares the number of hourly events with gusts exceeding 15 m/s that occurred during 2012 with the number that were detected with in the WRF simulations utilizing the ECMWF parameterization, as a function of the finest resolution employed. An average of 800 high gust events occurred at each tower, with relatively little variation among sites. All simulations for all towers undercounted the frequency of gust events. For two towers in regions 2 and 3, implementing the 3.3-km domain resulted in a significant improvement in the probability of detection. The extra expense involved with the 1.1-km domain does not appear to be justified, and thus we conclude that the 3.3-km resolution suffices.

Tower	Geographical region	Height of anemometer analysis	Number of events with gust > 15 m/s	Number of events detected d01 30-km	Number of events detected d02 10-km	Number of events detected d03 3.3-km	Number of events detected d04 1.1-km
AS	3)	101m	879	188	181	412	417
MC	1)	101m	732	250	302	366	381
JI	2)	98 m	901	586	357	629	590
RCH	2)	74 m	618	393	434	424	389
RM	1)	101m	876	381	504	511	510
CR	3)	101m	597	149	198	199	204

Table 2. UTE towers, and the number of events with gusts exceeding 15 m/s, determined using the ECMWF method.

The local vertical stability at each tower is both directly assessed from differential temperature measurements (using thermometers mounted near tower top and bottom) and computed from the WRF simulations. Four stability classes are defined empirically as:

1. Unstable when $\frac{\delta T}{\delta z} < -0.01$ °C/m, red in plots.
2. Slightly unstable when 0 °C/m $> \frac{\delta T}{\delta z} > -0.01$ °C/m, magenta in plots.
3. Slightly stable when 0.01 K/m $> \frac{\delta T}{\delta z} > 0$ °C/m, blue in plots.
4. Stable when $\frac{\delta T}{\delta z} > 0.01$ °C/m, green in plots.

Apart from an inability to capture absolutely unstable conditions, the WRF model appears to reproduce measured stability well, at least in bulk. One way of appreciating this is presented in Figures 8, 9 and 10. The top row presents simulated vs. observed gust for each tower, differentiated by stability. For each tower, the panel labeled a) classifies stability based on the model, while b) employs measured values. The color patterns are very similar.

The bottom rows of Figures 8, 9 and 10 presents simulated PBL depth vs. observed gust, again color-coded by both WRF and measured stability. As anticipated, the PBL is deeper when the stability is lower, and again the largest gusts are obtained during those conditions. Taken together, our analysis suggests that the model is reasonably capturing the mean wind and stability, and the primary deficiency comes from underestimating the GF during marginal conditions. Thus, we now attempt to more directly incorporate stability information into the ECMWF gust parameterization.

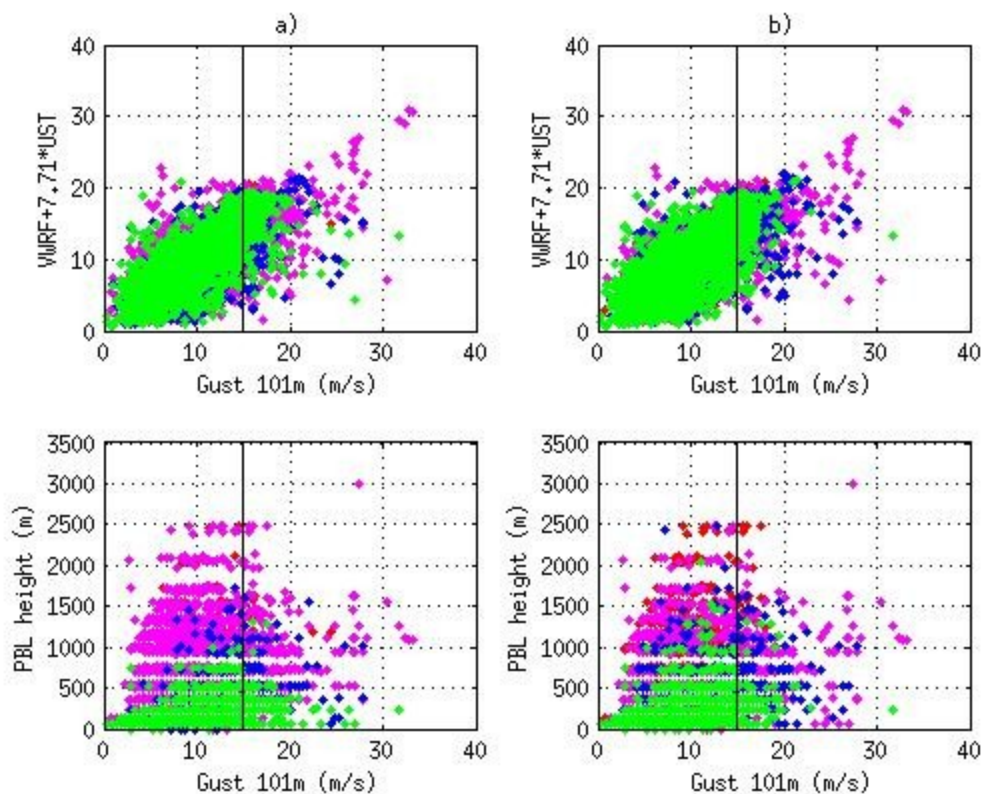


Figure 8. Gusts and PBL heights at tower RM, color-coded with respect to a) stability forecasted with WRF, and b) measured stability. Note that WRF-derived gusts are shown in the top row's vertical axes.

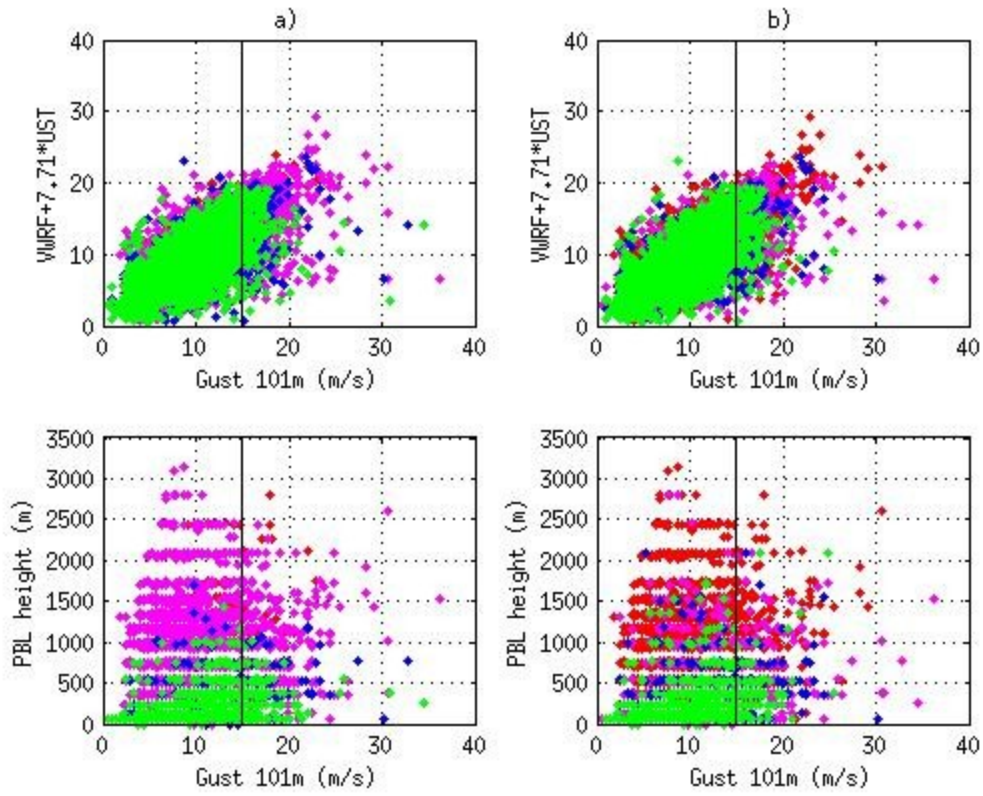


Figure 9. Gusts and PBL heights at tower AS, color-coded with respect to a) stability forecasted with WRF, and b) measured stability. Note that WRF-derived gusts are shown in the top row's vertical axes.

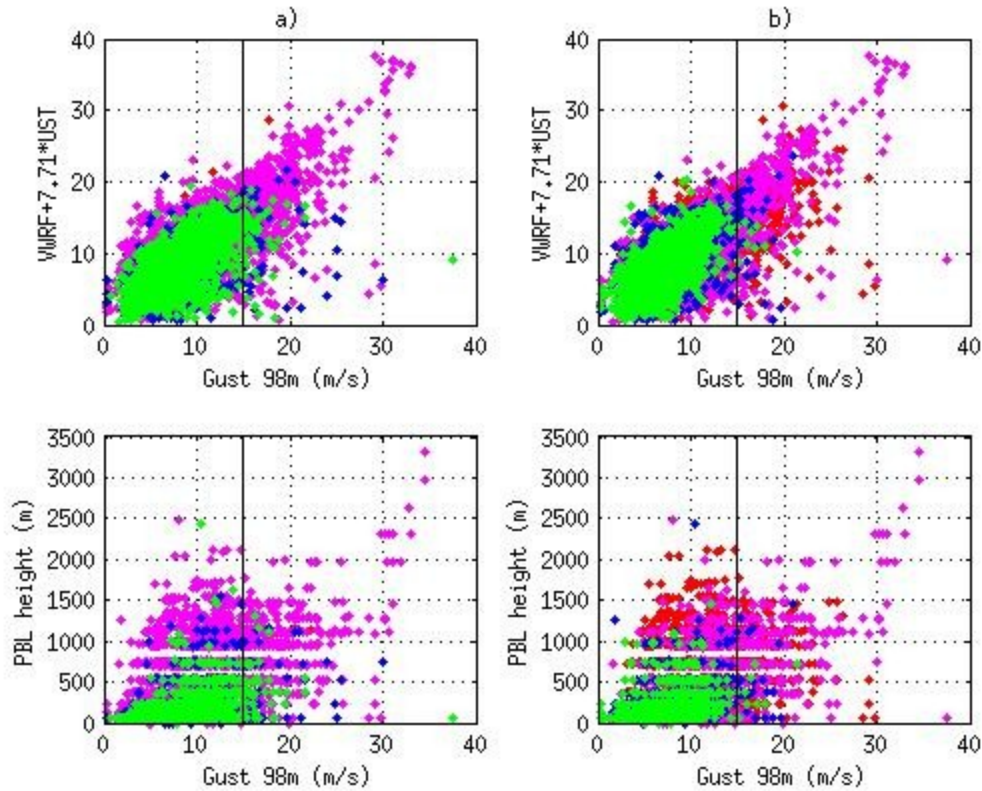


Figure 10. Gusts and PBL heights at tower JI, color-coded with respect to a) stability forecasted with WRF, and b) measured stability. Note that WRF-derived gusts are shown in the top row's vertical axes.

5 A modified gust parameterization

5.1 Description of modified gust parameterization

With the goal of incorporating forecasted stability information into a gust parameterization, we start by thinking in terms of turbulent gust generation by the vertical shear of the horizontal wind $\frac{\delta V}{\delta z}$ and by buoyancy forces represented by the vertical gradient of the temperature $\frac{\delta T}{\delta z}$. From the simulations, we compute the vertical temperature gradient between the second and first model levels (being roughly 92 and 27 m AGL), noting that these roughly correspond to heights at which the tower thermometers have been mounted (see Table 1). The vertical shear is computed between the tenth (about 1563 m AGL) and second levels, the latter being close to anemometer height. This is an attempt to represent the vertical scale of the largest eddies within the unstable convective PBL [17].

Motivated by the data, a different model for the gust factor GF is proposed for each of three windspeed-dependent classes:

for $\bar{V} < 5 \text{ m/s}$

$$GF = \frac{3.8 + 0.74\bar{V}}{\bar{V}} + \frac{k_{1v} \frac{\delta V}{\delta z} - k_{1T} \frac{\delta T}{\delta z}}{\bar{V}} \quad (2)$$

for $5 \text{ m/s} \leq \bar{V} < 15 \text{ m/s}$

$$GF = 1.45 + \frac{k_{2v} \frac{\delta V}{\delta z} - k_{2T} \frac{\delta T}{\delta z}}{\bar{V}} \quad (3)$$

for $\bar{V} \geq 15 \text{ m/s}$

$$GF = 1.33 \quad (4)$$

where k_{1v} , k_{2v} , k_{1T} , k_{2T} are positively-valued constants. Values for these constants and other coefficients in (2) and (3) were determined in the following way, expressed for the general gust (rather than GF) form of the equation given in (5). Regression equations involving an intercept, the mean wind \bar{V} , and the stability and shear terms were constructed for four towers separately, for the full range of data as well as for the subsets of $\bar{V} < 5 \text{ m/s}$ and $5 \leq \bar{V} \leq 15 \text{ m/s}$ (Table 3). The equations were then combined to form versions that could apply to all four locations simultaneously. In this process, some empirical adjustments were made to the coefficients to improve MAE and the detection of gusts exceeding 15 m/s, resulting in the values listed in the far right column of Table 3. The intercept term in (2) helps compensate for an excess of low windspeed conditions in the WRF simulations; this term was judged unnecessary for (3).

$$g = V_0 + k\bar{V} + k_v \delta V - k_T \delta T \quad (5)$$

	RM	AS	MC	JI	
			For all \bar{V}		
k (nondimensional)	1,03	1,00	0,99	0,95	
V0 (m/s)	2,78	3,23	2,80	2,74	
k_v (nondimensional)	0,13	0,18	0,16	0,18	
-k_T (m/s/°C)	-0,34	-0,34	-0,25	-0,36	
			For $\bar{V} < 5 \text{ m/s}$		Coefficients
k (nondimensional)	0,70	0,96	0,65	0,63	0,74
V0 (m/s)	3,97	3,31	4,19	3,84	3,80
k_v (nondimensional)	0,15	0,20	0,12	0,19	0,17
-k_T (m/s/°C)	-0,30	-0,21	-0,26	-0,02	-0,20
			For $5 \leq \bar{V} < 15 \text{ m/s}$		
k (nondimensional)	1,35	1,37	1,30	1,25	1,45
k_v (nondimensional)	0,15	0,20	0,17	0,16	0,18
-k_T (m/s/°C)	-0,39	-0,41	-0,26	-0,45	-0,35

Table 3. Coefficients from equation (5) determined for towers RM, AS, MC and JI, from year 2012 data, and the coefficients selected for model equations (2) and (3).

Although the ECMWF parameterization employs the friction velocity, which is a measure of vertical wind shear (within the surface layer), the above represents a fundamentally different approach to modeling gusts, one that is motivated by the data collected at these three towers. The vertical shear is taken through a deeper layer, and the k_{1v} and k_{2v} terms recognize that the same vertical shear could have different influences on gustiness depending on how fast the sustained winds are at anemometer

level. The $\frac{\delta T}{\delta z}$ term acts to enhance or suppress gustiness, depending on the sign of the vertical temperature gradient; when positive, the stability acts to suppress whatever mechanical turbulence that may be generated by the vertical shear. Note that for

high wind speeds $\bar{V} \geq 15 \text{ m/s}$, the gust factor reverts to the observed asymptotic value of 1.33 seen in the observations (Figure 15, left column).

5.2 Discussion of modified gust parameterization

Figure 11 show in left column computed vertical velocity difference δV between model levels ten and two (m/s), and the right column the computed temperature difference δT ($^{\circ}\text{C}$) between levels two and one, all plotted against the WRF wind representative of anemometer height (the second model level) for each of the three towers. The data are again color-coded by stability diagnosed in the simulations. (As noted earlier, the WRF model does not permit superadiabatic layers.) Figure 12 presents a subset of these observations, which affords a closer look at how they influence the parameterized gusts. Note the range is restricted to $0 < V < 15 \text{ m/s}$, and differences have been multiplied by k_{2v} , and k_{2T} and respectively, so they represent gust corrections to equation (3), effectively adjusting the default gust factor of 1.45 up or down. For winds exceeding 15 m/s, the gust factor is fixed at 1.33.

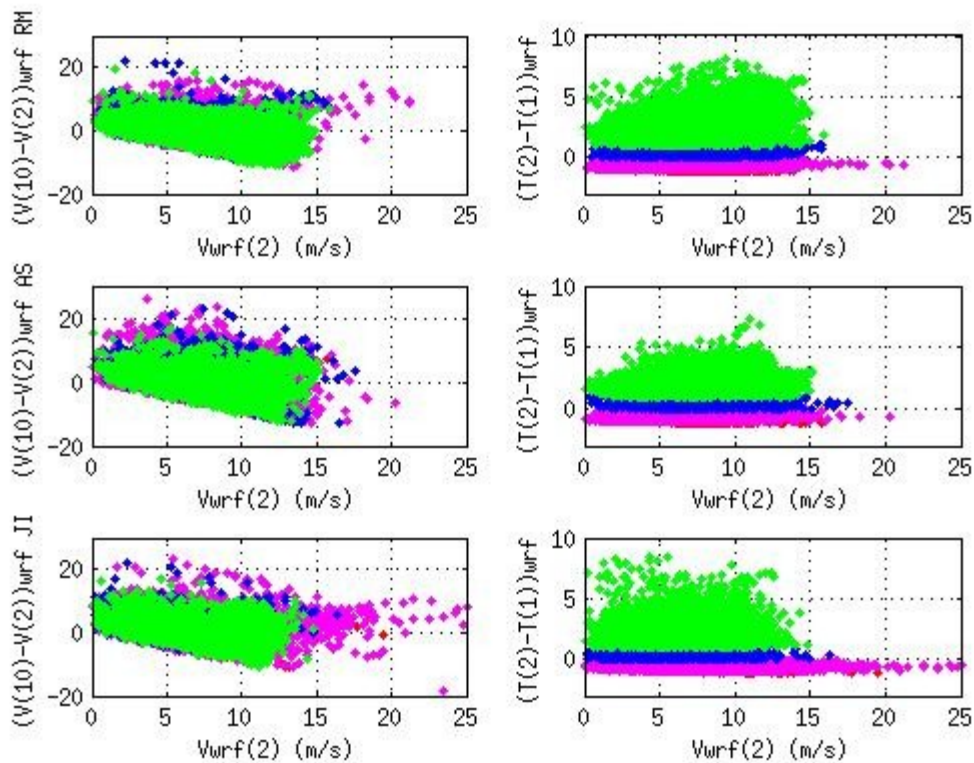


Figure 11. Scatterplots of the vertical shear (at left, expressed as windspeed difference in m/s between model levels 10 and 2) and stability (at right, expressed as temperature difference in $^{\circ}\text{C}$ between model levels 2 and 1) vs. windspeed at level 2, color-coded with respect to stability forecasted with WRF, for towers RM, AS and JI.

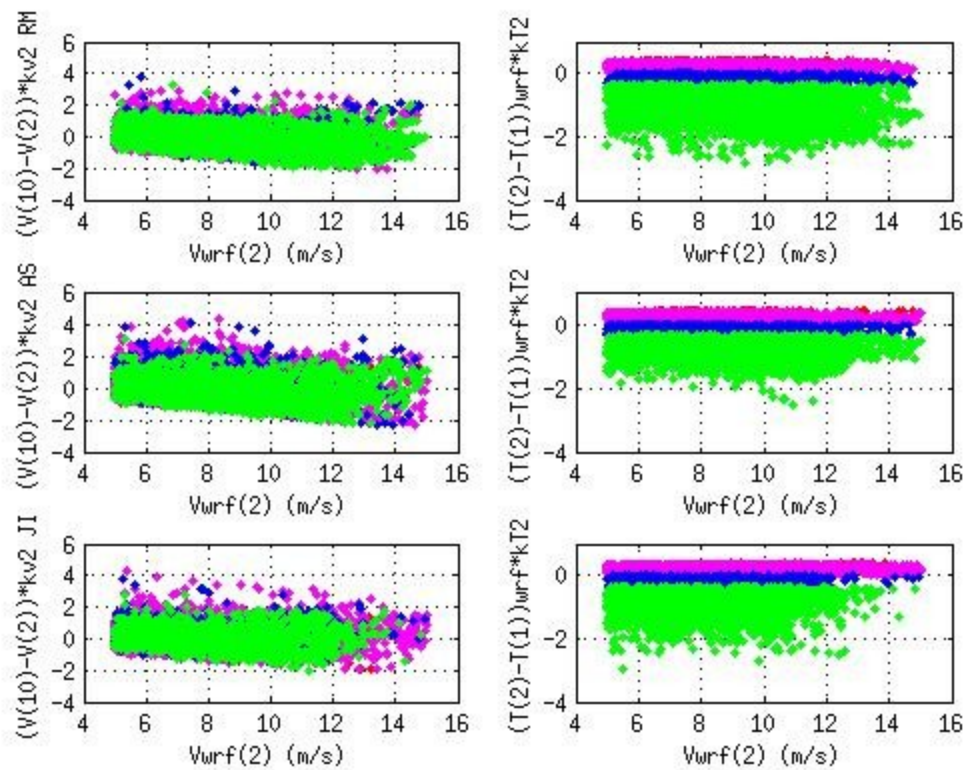


Figure 12. As in Fig. 11 but for windspeed data restricted to the range between 5 and 15 m/s. Vertical axes multiplied by coefficients k_2V and k_2T , which converts speed and temperature information to gust correction terms.

When δV is negative, the simulated wind speed decreases above tower level, especially when the anemometer level winds are strong. Under these conditions, the term $\frac{\delta V}{\delta z}$ is acting to reduce the gust predicted at turbine height. This often occurs when the atmosphere is stable (green markers). However, even when the atmosphere is less stable, the shear term can act to reduce the gusts, especially at tower JI. The histograms in Fig. 13 display the relative frequencies at which the shear correction is acting to diminish or enhance the gust. When the atmosphere is at least slightly unstable (left column), the roughly normally distributed frequencies center around zero, indicating that positive and negative corrections are equally likely.

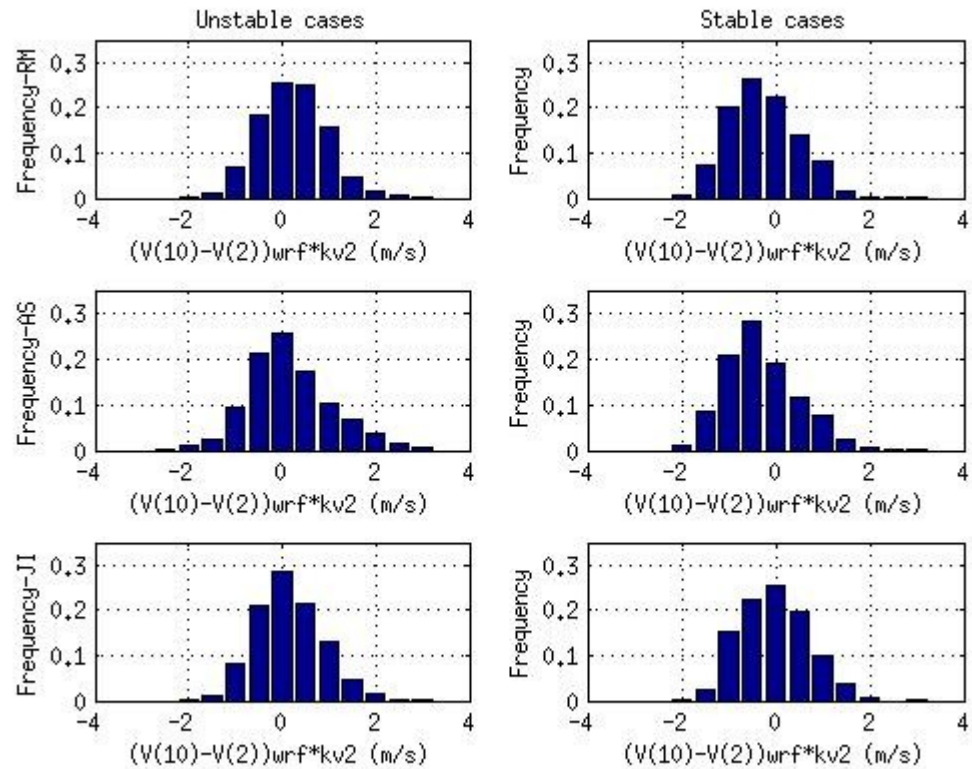


Figure 13. Frequency of vertical windspeed and temperature differences as a function of stability class (slightly unstable at left, stable at right) for towers RM, AS, and JI.

This means that in half the cases, the new parameterization is enhancing the gust, helping to address the gustiness deficiency in marginal cases noted earlier. For stable conditions, the distributions are clearly shifted towards gust suppression, except at the coastal tower JI. The temperature difference correction term (right hand columns in Figs. 11 and 12) acts to reduce the gusts when the atmosphere is strongly stable. Otherwise, it has little effect.

5.3 Comparison of ECMWF model and modified gust parameterization

Figure 14 (left column) presents a scatterplot of observed gust vs. sustained wind for towers RM, AS and JI, color-coded by vertical stability measured at the towers. The gust factor represents the slope between these two variables. For a given mean wind, the gust is larger as the stability is decreased, resulting in a somewhat higher GF. The scatter is greater for intermediate sustained wind speeds (between 5 and 15 m/s), especially when the stability is marginal.

The remaining two columns relate the gusts from the ECMWF and new parameterizations with the observed gusts, color coded with respect to simulated stability. Although there is a large amount of scatter, the 1:1 correspondence line suggests both parameterizations do a reasonable job of representing the gusts observed near 100 m.

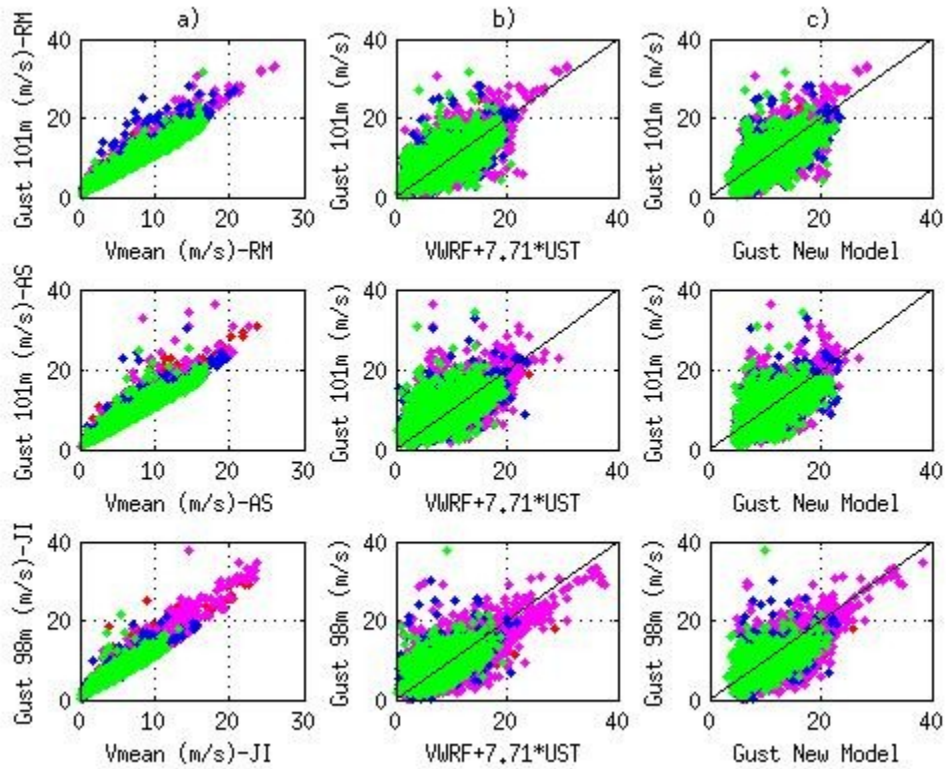


Figure 14. Scatterplots for towers RM, AS, and JI of: a) observed mean velocity vs. gust; b) WRF simulated gust using ECMWF formula vs. observed gust; and c) WRF simulated gust using modified gust parameterization vs. observed gust. In a), data are color-coded by vertical stability measured at the towers; in b) and c), data are color-coded with respect to stability forecasted with WRF.

However, there is a systematic bias in the ECMWF parameterized gusts that is revealed when the wind is plotted against the computed GF (Fig. 15). In the observations (left column), we see that while gust factors tend to decrease with increasing sustained wind speed, there is a fair amount of scatter, especially at intermediate wind speeds. This reveals that sizable gusts are possible when the atmosphere is less stable. This is not captured in the ECMWF parameterization (middle column), which does not anticipate that larger gust factors are possible when the simulated atmosphere is what we termed slightly unstable. The parameterization tends to underpredict the largest gusts (especially at JI, the tower nearest the Atlantic Ocean). Of particular concern are the data points residing above the correspondence line when the WRF-forecasted wind is less than 20 m/s or so, which are the (all too numerous) missed cases noted in Table 2.

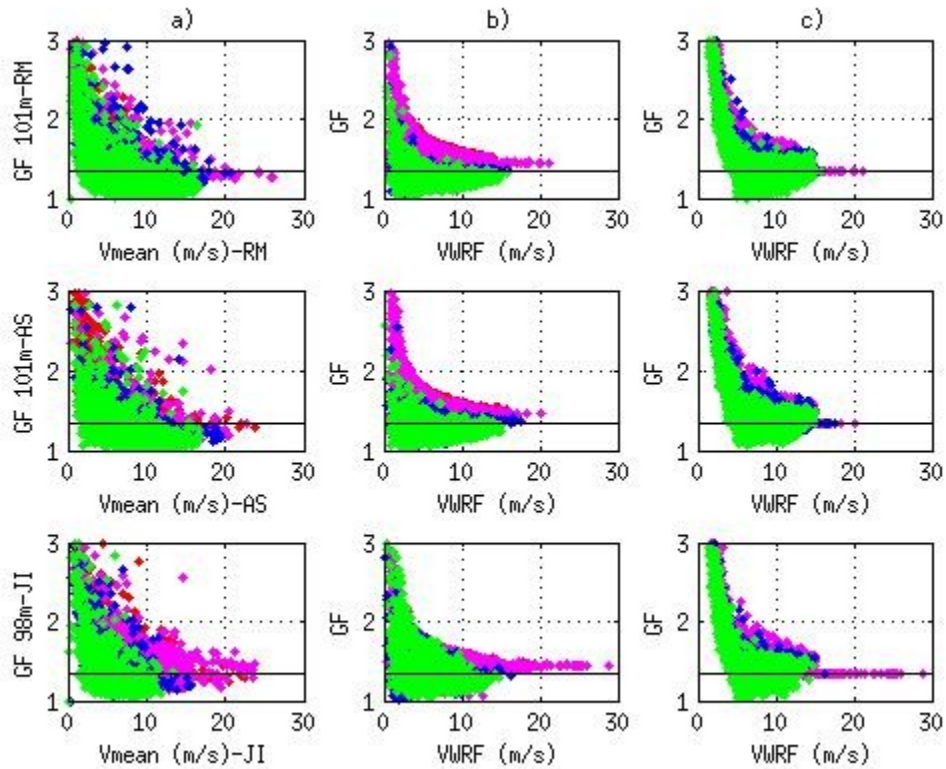


Figure 15. Scatterplots for towers RM, AS, and JI of: a) observed mean velocity vs. observed gust factor; b) WRF simulated mean velocity vs. gust factor computed with ECMWF equation; and c) WRF simulated mean velocity vs. gust factor computed using modified gust parameterization. In a), data are color-coded by vertical stability measured at the towers; in b) and c), data are color-coded with respect to stability forecasted with WRF..

In contrast, the new parameterization (right column of Figs. 14 and 15) has more spread towards larger gust factors for these marginal cases. The modified model is capable of identifying larger gusts when the stability is slightly stable (colored blue). These gusts were completely absent previously (middle column), which had no discernible overlap between marginally stable and marginally unstable (colored magenta) conditions. The consequence of limiting the high-wind GF via (4) is also seen.

Table 4 summarizes the number of hourly events with observed gusts (g) exceeding 15 m/s during 2012 with the number that were detected within the WRF simulations ($gwrf$) utilizing the ECMWF or proposed parameterizations. Again, the frequency of high wind events is underrepresented in the 3.3 km simulations the three towers. However, the proposed strategy captures more of them, at the cost of slightly more false alarms. The mean absolute errors (MAEs) for the two approaches are comparable, being improved at inland tower AS.

	Vwrf+7.71ust				Model proposed		
	$g > 15$ m/s	$g > 15$ m/s & $gwrf > 15$ m/s	$gwrf > 15$ m/s	MAE (m/s)	$g > 15$ m/s & $gwrf > 15$ m/s	$gwrf > 15$ m/s	MAE (m/s)
AS	879	412	851	2,20	469	1071	2,07
JI	901	629	1167	2,26	673	1392	2,29
RM	876	511	940	2,06	572	1110	2,02
		Real case	False case		Real case	False case	
		46,87%	51,59%		53,36%	56,21%	
		69,81%	46,10%		74,69%	51,65%	
		58,33%	45,64%		65,30%	48,47%	

Table 4. Number of events with gusts higher than 15 m/s, and mean absolute error for the year 2012.

6 Conclusion

This study analyzed wind measurements made for wind energy in Uruguay, focusing on mean winds and gusts near turbine height (~ 100 m). Stability was directly measured at the towers using thermometers mounted at different heights. At three representative towers, selected to represent three distinct regions of the country, the gust magnitudes and gust factors both increase as the atmosphere becomes less stable. As the mean wind increases, however, the gust factor converges on a stable value of about 1.33.

WRF simulations are made in which the theory-based ECMWF gust parameterization is applied to predicted mean winds to yield gust forecasts. Overall, improving resolution past about 3 km does not result in better simulations in this generally grassy, gently rolling terrain. The model appears to provide reasonable reconstructions of the mean wind and vertical stability, and the variation of gust factor with the mean wind, but tend to underforecast large gust episodes at all locations examined. Our analysis suggests that more extreme gust factors are underestimated in marginal stability conditions, suggesting that a more direct influence of stability could improve the gust forecasts.

The modified gust parameterization proposed in this work better captures gusts occurring in marginal stability conditions for intermediate wind speeds. The refined parameterization could be employed within a probabilistic approach to provide better advanced warning of wind events that could affect wind energy production.

ACKNOWLEDGMENTS

This work was supported by agreement between the Administración Nacional de Usinas y Trasmisiones Eléctricas (UTE) and the School of Engineering UdelaR, as well as project ANII FSE-2011-6562.

References

- [1] <http://www.dinama.gub.uy/sia/sia/map.phtml>
- [2] Cornalino Eliana, Martín Draper. Planning the distribution of wind farms in Uruguay in order to optimize the operability of large amounts of wind power. EWEA 2012 Annual Event Monday 16 - Thursday 19 April 2012 | Bella Center, Copenhagen, Denmark <http://www.ewea.org/annual2012/>
- [3] Skamarock, 2008 NCAR/TN 475+STRNCAR TECHNICAL NOTE June 2008 A Description of the Advanced Research WRF Version 3
- [4] Kaimal, J. C., J. J. Finnigan, Atmospheric Boundary Layer Flows. Their Structure and Measurement, Oxford University Press 1994.
- [5] J.C Kaimal, J. C. Wyngaard, D. A. Haugen, O. R. Coté, Y. Izumi, S. J. Caughey, and C. J. Readings, 1976: Turbulence Structure in the Convective Boundary Layer. *J. Atmos. Sci.*, **33**, 2152–2169.
- [6] Otávio C. Acevedo and David R. Fitzjarrald. 2001 The Early Evening Surface-Layer Transition: Temporal and Spatial Variability. *Journal of the Atmospheric Sciences*: Vol. 58, No. 17, pp. 2650-2667.
- [7] Takle, E. S., 1983: Climatology of superadiabatic conditions for a rural area. *J. Climate Appl. Meteor.*, **22**, 1129–1132.
- [8] Czarnetzki, A. C., 2012: Persistent daytime superadiabatic surface layers observed by a microwave temperature profiler. Preprints, 37th Natl. Wea. Assoc. Annual Meeting, Madison, WI, Natl. Wea. Assoc., P2.55.
- [9] Gonzalo Abal, Mauro D' Angelo, José Cataldo, Alejandro Gutiérrez. Mapa Solar del Uruguay Versión 1.0 Memoria Técnica. 2011. ISBN 978-9974-0-0847-2.
- [10] Stull, Roland B. An introduction to boundary layer meteorology, Kluwe Academic Publishers, London 2003.
- [11] IFS DOCUMENTATION Cy37r2Operational implementation 18 May 2011 PART IV: PHYSICAL PROCESSES
- [12] Collins W.D et al 2004: Description of the NCAR Community Atmosphere Model (CAM 3.0), NCAR Technical Note, NCAR/TN-464+STR, 226pp
- [13] Lin, Y.-L., R. D. Farley, and H. D. Orville, 1983: Bulk parameterization of the snow field in a cloud model. *J. Climate Appl. Meteor.*, **22**, 1065-1092.
- [14] Chen, F., and J. Dudhia, 2001: Coupling an advanced land-surface/ hydrology model with the Penn State/ NCAR MM5 modeling system. Part I: Model description and implementation. *Mon. Wea. Rev.*, **129**, 569?585.
- [15] Kain, J. S., 2004: The Kain-Fritsch convective parameterization: An update. *J. Appl. Meteor.*, **43**, 170?181.
- [16] Mellor, G. L., and T. Yamada, 1982: Development of a turbulence closure model for geophysical fluid problems. *Rev. Geophys. Space Phys.*, **20**, 851-875.
- [17] John C. Wyngaard, 1985: Structure of the Planetary Boundary Layer and Implications for its Modeling. *J. Climate Appl. Meteor.*, **24**, 1131–1142. doi: [http://dx.doi.org/10.1175/1520-0450\(1985\)024<1131:SOTPBL>2.0.CO;2](http://dx.doi.org/10.1175/1520-0450(1985)024<1131:SOTPBL>2.0.CO;2)